

Performance evaluation of a novel gamma transmission micro-densitometer for PIE of nuclear fuel

L. Senis^{a,*}, V. Rathore^a, P. Andersson^a, K. Johnson^b, D. Jäternäs^b, C. Losin^b, D. Minghetti^b, J. Wright^c, D. Schrire^d

^a Division of Applied Nuclear Physics, Department of Physics and Astronomy, Uppsala University, Sweden

^b Studsvik AB, Nyköping, Sweden

^c Westinghouse Electric Sweden AB, Västerås, Sweden

^d Vattenfall Nuclear Fuel AB, Stockholm, Sweden

ARTICLE INFO

Keywords:

Gamma-transmission densitometry
Post-irradiation examination
Nuclear fuel inspection

ABSTRACT

Collimated Gamma Transmission Micro-Densitometry (GTMD) is a novel technique proposed to investigate local density variations of nuclear fuel in PIE, with a high spatial resolution. In this work, the first experimental tests of a gamma micro-densitometer are presented and the performance is characterized. The experimental procedures are described, including the aligning process and the calibration methodology. The results demonstrated that for the calibration samples with a thickness above 5 mm, a local density was obtained with a maximum discrepancy of about 2% and a spatial resolution of about 280 μm . The setup was used for the first test on an irradiated ADOPTTM fuel pellet slice. From the measurement, an average bulk density of about 9.58 g/cm³ was calculated and local density features were observed, possibly related to rim effects or the presence of local cracks. The information acquired also presented valuable information for possible improvements in the setup's performance.

1. Introduction

During irradiation, the nuclear fuel matrix accumulates irradiation defects, and solid, as well as gaseous fission products, which result in increased porosity, lower bulk density, and thus a net swelling of the fuel (Schrire et al., 1998). The steep radial thermal gradient also contributes to the accumulation of defects at high burnup, generating microstructural changes (Guerin, 2012; Une et al., 1992; Baron et al., 2009; Lozano et al., 1998; Noirot et al., 2008). This is further enhanced in the pellet rim, where the lower temperatures are insufficient for thermal recovery leading to the appearance of dense microscopic porosity, and nanograin size subdivision (Baron and Hallstadius, 2012). Because of this effect, in the pellet periphery, the density has been observed to decrease up to tens of percent (Spino et al., 2005; Spino et al., 1998). The combination of the described effects generates a progressive variation in the radial local density, which makes high-resolution densitometry methods, such as GTMD, of interest.

Gamma transmission densitometry (GTD) is a non-destructive technique, which provides information on the bulk density of a sample thanks to the use of an external gamma-ray source (Kumara et al., 2010;

Lassahn et al., 1979; Tjugum et al., 2002; Affonso et al., 2015; Reilly et al., 1991). Due to the interaction of gamma radiation with matter, an attenuation of the outbound flux can be detected, and this can be used to calculate the sample density. The difference in the attenuation is dependent on the gamma energy, and the attenuation coefficient and thickness of the sample material, as described mathematically by the Beer-Lambert law (Swinehart, 1962). In this application, a collimator is used to limit the field of view of the detector and allow for local measurement of the density. The GTD technique has also been used to investigate the density profile in high burnup fuel, as well as used to obtain a tomographic reconstruction of the linear attenuation coefficient (Caruso et al., 2008; Caruso, 2007). This latter application also had practical implementation in gamma emission tomography (Caruso et al., 2009).

A novel collimated densitometry technique was proposed in Ref. (Senis et al., 2021) to investigate the variation of density in nuclear fuel samples post-irradiation, which typically decreases as a consequence of swelling (Schrire et al., 1998; Daniel et al., 1962; Van Brutzel et al., 2015). In the study, a resolution in the order of a hundred microns is aimed to resolve the density variation of the fuel matrix in the rim

* Corresponding author.

E-mail addresses: lorenzo.senis@physics.uu.se (L. Senis), peter.andersson@physics.uu.se (P. Andersson).

<https://doi.org/10.1016/j.anucene.2023.109783>

Received 13 December 2022; Received in revised form 7 February 2023; Accepted 23 February 2023

0306-4549/© 2023 The Author(s). Published by Elsevier Ltd. This is an open access article under the CC BY license (<http://creativecommons.org/licenses/by/4.0/>).

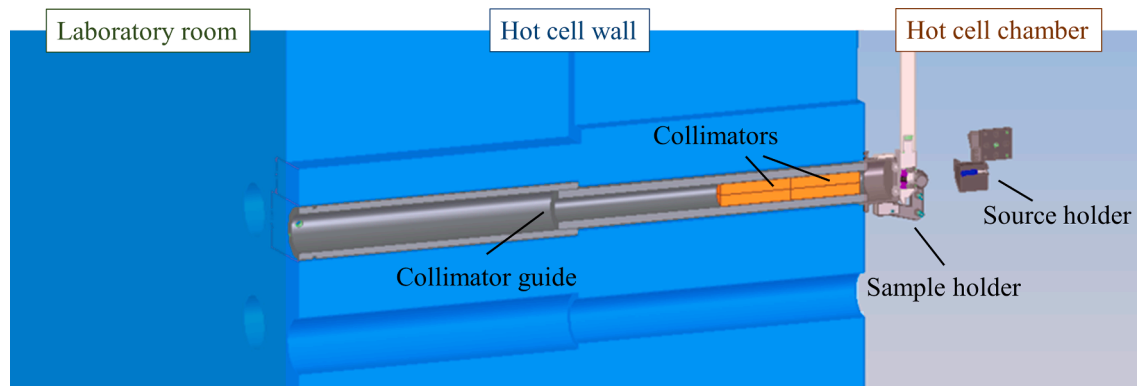


Fig. 1. A CAD representation of the setup as positioned in the hot cell wall and the hot cell chamber. From the right, the source holder is positioned in front of the slit of the collimator. The sample holder is positioned in a dedicated mechanism that allows the vertical movement of the sample. The collimators are positioned at the end of the collimator guide and their positions are fixed using screw holes.

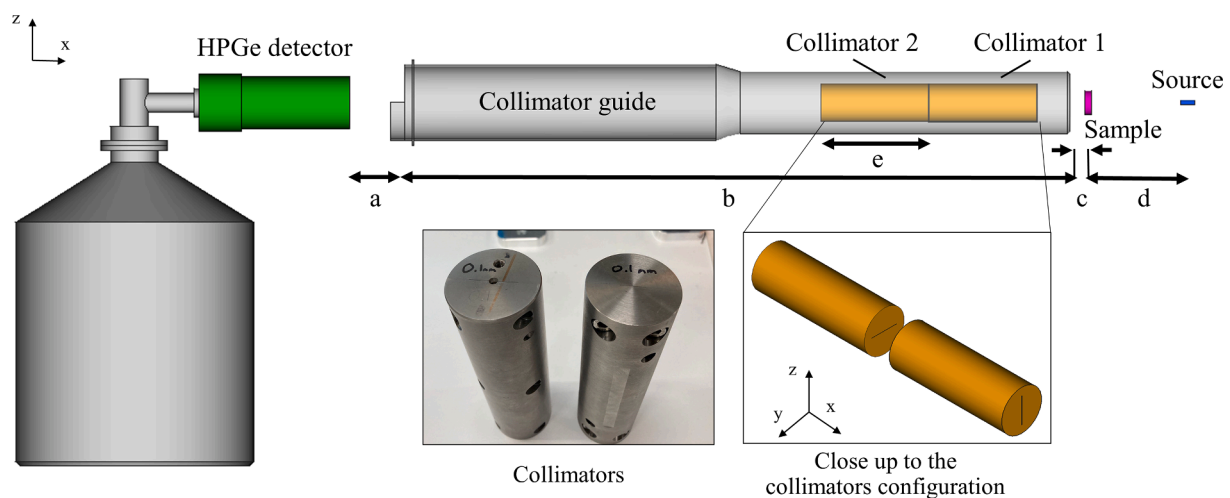


Fig. 2. Simplified not-to-scale side view of the setup presented in Fig. 1. An HPGe detector is positioned at the entrance of the hot cell wall aperture where a tube is used as a collimator guide. Collimators 1 and 2 are inserted into the tube and separated from the hot cell chamber through a steel separator. The sample is positioned in a sample holder which is adjacent to the separator and moved among the z-direction within a guide. The source is positioned in a source holder that can be moved among all three directional axes.

region where, due to the “high burnup structure” (Rondinella and Wiss, 2010; Spino et al., 1996), a drop in the density up to tens of percent could be expected (Spino et al., 2005). Such information is of interest to nuclear fuel operators and producers to enable accurate modeling of the fuel performance during irradiation, such as heat transfer (Lee et al., 2001).

A detailed description of the collimated gamma micro-densitometry method has been extensively presented in a previous publication. In Ref. Senis et al. (2021), the theory of the technique is presented, and it was shown through simulations that resolution in the 100- μm region is feasible. The study demonstrated that for the setup proposed a relative error of less than 1% in the density measurement can be obtained with a spatial resolution of about 110 μm , and 1 h of investigation per position using the lower energy line emitted by a 1 TBq Co-60 source (but with the same approach, also the other gamma line can be used as well). The study only considered as a source of uncertainty the counting statistics of the measurement of attenuated and unattenuated intensity.

To build the densitometer, the design suggested has been modified to be usable in the hot cell laboratory of Studsvik in Nyköping. The new design, presented in Section 2.1, was made and assembled in the laboratory, ready to be used for post-irradiation examination of nuclear fuel. This work presents the results of the first experimental campaign, with the scope to evaluate the performance of the current design in terms of

Table 1

Selection of dimensional parameters of the setup highlighted in Fig. 2. (*) It can be noted that the parameter “a” does not represent a sensitive parameter in the setup due to the difference in sizes between the detector and the gamma beam. In fact, the beam itself will be fully contained in the detector even at bigger distances.

Fig. 2 parameters	Distance [mm]
a – Detector-collimator guide distance (*)	100
b – Collimator guide length	1230
c – Collimator-source distance	5
d – Sample-source distance	100
e – Collimator length	130

density accuracy and spatial resolution. In addition, the first examination of irradiated nuclear fuel was performed.

2. Experimental campaign

2.1. Apparatus

The setup earlier proposed in Section 2 of Ref. (Senis et al., 2021) has been used as a reference to realize the prototype in Studsvik hot cell laboratories as shown in Figs. 1 and 2, while the dimensions are reported

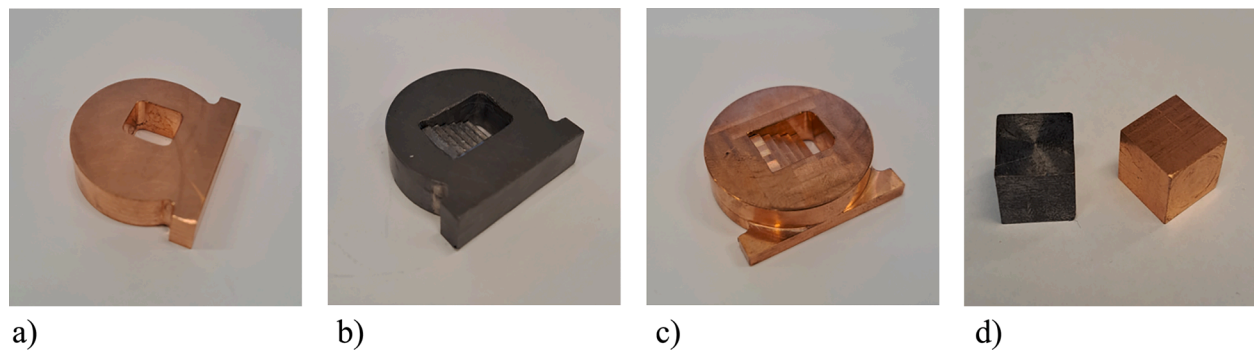


Fig. 3. a) Single edge sample b) lead sample c) copper sample d) standard samples.

in Table 1. A few parts of the setup have been subjected to changes, for practical reasons. A change has been applied in the collimation, where in Ref. Senis et al. (2021), a collimator made in pure tungsten was modeled in the simulations but in the real setup, the so-called densimet® alloy was used in its place (Pasalic et al., 2014). This tungsten alloy is easier to machine; however, its density is a few percent lower than pure tungsten. For this setup, a combination of two densimet® collimators (shown in Fig. 2), each with a slit size of $10 \times 0.1 \times 130$ mm, has been used. This was deemed easier to machine than a sub-millimetric square slit in a single collimator block. The combination of the two results effectively in obtaining a 0.1×0.1 mm square slit, by positioning the two slits in a cross form (as shown in Fig. 2). The lower density of the densimet® alloys is expected to partially degrade the resolution of the setup, because of a higher probability of leakage of gamma rays through corners of the slit. In addition, the Co-60 source used for this measurement campaign had an activity of about 0.7 TBq, which is smaller activity than the planned source (Senis et al., 2021). It can be noted that due to the decay of the source nuclide, there is an inevitable variation of the activity, and the source will occasionally need replacement.

2.2. Setup preparation procedures

2.2.1. Alignment of source with the collimator slit

Alignment of the setup was performed in the following manner:

- 1) Both collimators (1 and 2) were inserted in the collimator guide (see Figs. 1 and 2), firstly with both slits aligned vertically (z-axis direction).
- 2) The source was positioned in the source holder and moved along the x-axis as close as possible to the wall aperture. In fact, having the source closer to the collimators would be a benefit, having a stronger signal and also facilitating the alignment process. Some mechanical limitations are present, such as the range of movement of the source holder, but there is also the need for space to manipulate the holder without accidentally hitting it during the maneuvers.
- 3) The source was moved manually using remote manipulators in the y-direction while the live count rate of the detector was monitored until the maximum signal has been observed.
- 4) Fixed in the y-position, the second collimator (collimator 2 in Fig. 2) was rotated by 90° , and the source was moved again but in the z-direction. When the new maximum signal reached the alignment, the procedure was considered completed.

It can be noted that the procedure was performed manually (by remote manipulators), therefore it is subject to some degree of variation. A 4 h measurement was used as a reference to obtain the unattenuated flatfield intensity, which is required for the density determination according to Beer's law. During the measurement campaign, additional measurements of the flat beam, of about 1 h, have been performed to test its stability, the results of which are discussed in Section 4. A

Table 2

The thicknesses of the different steps of the stairs pattern. The errors included are based on the sensitivity of the micrometer, 0.01 mm.

Material		Copper	Lead	ADOPT™-UO ₂
Step thickness [mm]	T1	3.04(1)	3.07(1)	6.44(1)
	T2	4.04(1)	4.06(1)	
	T3	5.04(1)	5.05(1)	
	T4	6.03(1)	6.06(1)	
	T5	7.03(1)	7.06(1)	
Standard's density [g/cm ³]		8.88(2)	11.31(2)	10.18(3)

background measurement of 2 h was also performed, during which the source was removed from the sample holder.

2.2.2. Evaluation of spatial resolution

To quantify the resolution of the setup, an edge spread test was performed. This was done by scanning a sharp edge sample (Fig. 3a), with small steps (100-μm steps were the lower limit of the setup) and observing how the edge is smeared in the recorded profile, i.e. the Edge Spread Function (ESF) (Díaz et al., 2021). The spatial resolution was then calculated as the distance between the positions of 10% and 90% of the full contrast. The analysis of the ESF test is reported in more detail in Section 4.1.

2.2.3. Density calibration

The density calibration was performed using two calibration samples made of copper and lead, and their densities were compared using two standard methods. By comparison, we could evaluate deviations from the density determined by the densitometer, and account for them in the fuel measurements. The samples have been manufactured with a step-wise increase in thickness, resembling stairs, as seen in Fig. 3b and c. They present a solid object with an inner cavity with a stairs pattern. The steps of the stairs present different thicknesses to the transmitted gamma rays (reported in Table 2), which have been used to observe if deviations in the density value occur also due to different sample thicknesses. The densities used as standards were calculated as the ratio between the weight (measured with a scaler) and the volume of sample cubes machined from the same material of the samples (shown in Fig. 3d). The uncertainty considered for the standard comes from the sensitivity of the scaler and the micrometer used.

2.3. Irradiated fuel density profile

Once calibrated, the setup was used to acquire a density profile of a pre-irradiated accident tolerant fuel candidate, currently produced by Westinghouse called "ADOPT™" fuel (Hallman, 2020) (UO₂ with less than 1% of Cr and Al doping). The sample is a fuel slice (the cladding outer diameter at fabrication is 9.62 mm, while the fuel density after irradiation is 10.18 ± 0.03 g/cm³) with an accumulated burnup of 65 GWd/tU. The sample was stabilized in epoxy resin and cut with a

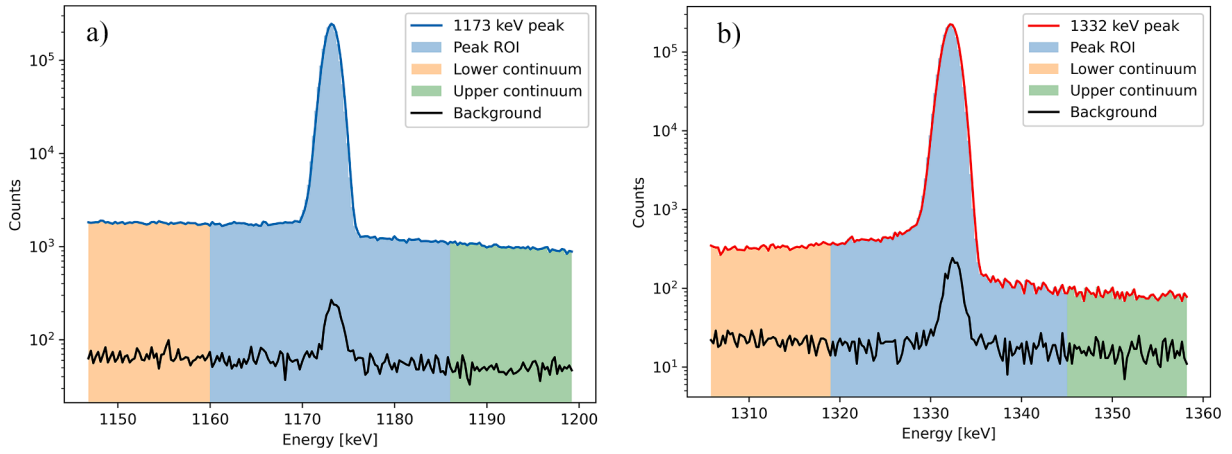


Fig. 4. a) In blue, the co-60 peak at 1173 keV of the flat beam spectrum, and in black the corresponding background spectrum. b) In red, the Co-60 peak at 1332 keV of the flat beam spectrum, and in black the corresponding background spectrum. For both spectra, the y-axes have been reported in the logarithmic scale.

nominal thickness of 6.44 mm. The sample has been scanned with a regular step of 100 μm and 1 h of measurement per step, covering the radius with some margin. The procedure used to analyze the fuel data and to localize the sample along the scanned axis is presented in more detail in Section 4.3.

3. Data analysis

For each measurement step, a gamma spectrum has been acquired and the peaks of Co-60 at 1173 keV and 1332 keV were analyzed, using the procedure proposed in Section 5 of Ref. Gilmore (2008) and applied as in Section III-C in Ref. Senis et al. (2022). In the analysis, the difference in acquisition time has been accounted for. The total count rate in the spectra was less than 2000 cps (also for the flat beam measurement) with a dead time below 4% that was corrected automatically by the acquisition system. A graphical illustration of the peak analysis is shown in Fig. 4, for the flat beam spectrum and the background spectrum. It can be noted that Co-60 peaks are present also in the background at the facility. Therefore, the peak background was evaluated and used for subtraction of all measurements of transmitted intensity through the collimator.

3.1. Correction coefficients

Correction factors have been applied to the model proposed in Eq. (1) from Ref. (Senis et al., 2021), to correct the deviation observed in Beer's law,

$$I = I_0 e^{-\frac{C_S C_U \mu_m \rho x}{C_D}} \quad (1)$$

The sample density, ρ , was then calculated as,

$$\rho = \frac{C_D \ln(I_0/I)}{C_S C_U \mu_m x}, \quad (2)$$

where I and I_0 represent respectively the attenuated and unattenuated gamma intensity, μ_m is the mass attenuation coefficient and x is the sample thickness. The correction factors introduced in Eqs. (1) and (2) are:

1. C_S , small angle scattering correction (for all samples).
2. C_U , burnup correction (for the fuel sample).
3. C_D , calibration standards correction (for the fuel sample).

3.1.1. Small angle scattering correction

This factor has been used to correct the mass attenuation coefficient,

obtained from the NIST-XCOM database (Berger et al., 2020). The database can include or exclude coherent scattering (Storruste and Tjóm, 1958; Schopper, 1957). Coherent scattering is characterized by a negligible energy loss and a small angle of deviation, potentially making this scattered component undistinguishable from the un-scattered signal. For many applications this effect might be negligible, affecting only a few percent of the gamma intensity, but for this densitometer application with a target of 1% precision, it is sufficient to introduce a bias, unless accounted for. In this application, where a tiny slit has been used, small deviations in the scattering angle may be sufficient for the gammas to be scattered in the bulk of the collimator and removed from the flux. Therefore, there may be a non-negligible probability that part of the coherent scattering could deviate enough to miss the detector, while the remaining part, still contributes to the full-energy peak.

The presence of coherent scattered gammas in the detector was investigated using a Monte Carlo approach. Using MCNP6 (Werner, 2017), a simplified geometry has been modeled to evaluate the full-energy contribution reaching the detector and compare it with Beer's law with or without coherent scattering. In the simulations, the source has been modeled as a point emitting a pen beam at 1173 keV and 1332 keV, pointed perpendicularly to the sample and the detector surfaces and centered to the collimator slit. The samples were modeled as a cylinder made with the same materials (copper, lead, or uranium dioxide) and its thickness varied among the dimensions reported in Table 2. The collimators have been modeled as a composition of two adjacent collimators made of densimet® with the same dimensions as described in Section 2.2.1. The detector has been modeled as a circular counting surface (using F1 photon tally functionality) at the detector position (about 1 m from the sample) and with a radius equal to the detector radius (30 mm).

The correction factor, $C_S = \frac{\mu_{w.o.}}{\mu_{MCNP}}$, was then calculated as the ratio between the mass attenuation factor obtained from NIST-XCOM without the coherent scattering, $\mu_{w.o.}$ and the mass attenuation factor obtained from MCNP simulations as,

$$\mu_{MCNP} = -\frac{\ln\left(\frac{I_{MCNP}}{I_{0,MCNP}}\right)}{\rho x} \quad (3)$$

where, $I_{0,MCNP}$ and I_{MCNP} are respectively unattenuated and attenuated gamma current in the simulations, ρ is the density of the standard sample material and x is its thickness. The factor C_S was then applied to Eq. (2) for the correction. The one standard deviation uncertainties reported in Tables 5 and 6 are calculated from the error propagation of the statistical uncertainties of the simulation.

Table 3

The coefficients used for the calculation of the burnup correction factor, C_U . The values have been obtained from Table 4 in Ref. (Atak et al., 2020) and used in the linear interpolation applied to Eq. (4).

Gamma energy [keV]	1000	1250	1500
a_0 [cm ² /g]	0.0772	0.0629	0.0554
a_1 [cm ² /g GWd/tU]	−1.8E-05	−1.1E-05	−0.8E-05

3.1.2. Burnup correction

During irradiation, the intense neutron flux changes the elemental composition of the fuel due to fission events and other transmutation reactions. These variations in the composition affect the physical properties of the material, such as its attenuation coefficient (Atak et al., 2020). The attenuation of irradiated fuel is lowered with the increase of the burnup because of the replacement of uranium by fission products of lower atom number. A correction factor, C_U , has been introduced to account for this decrease and calculated through the interpolation model proposed in Eq. (3) in Ref. (Atak et al., 2020). The coefficients reported in Table 3 (taken from Table 4 in Ref. (Atak et al., 2020)) have been used for linear interpolation; the function, f , depends linearly on the burnup, BU ,

$$f = a_0 + a_1 * BU, \quad (4)$$

and it is used to calculate the correction as

$$C_U = \frac{\mu_m}{f}, \quad (5)$$

where μ_m is the mass attenuation coefficient of uranium dioxide at $BU = 0$.

The correction has been applied assuming a homogeneous burnup of 65 GWd/tU among all the measured points in the fuel region. The corrections have been extracted from the linear interpolation (Eq. (4)) at the energies of interest (1173 keV and 1332 keV), using the function “interp1” available on Matlab. Using Eq. (5), the C_U factors have been calculated and reported in Table 6 of Section 5.

The uniform assumption used represents a simplification. It is known that the burnup varies slightly with the radial position and increases significantly in the high-burnup rim region. In this region, the burnup can be up to double the average value (Barlow, 1993). Using as an example a $BU = 120 \text{ GWd/tU}$, the correction C_U can be up to 1% higher than the values calculated using the burnup average. To consider such variation a method that measures the local burnup may in the future be coupled with the densitometer measurements, such as SEM-WDS or LA-ICP-MS analysis, to obtain a better correction factor. Nevertheless, applying the average burnup is considered a reasonable approximation at all positions save the rim, which may lead to a slight underestimation of transmission through this region.

3.1.3. Correction using the calibration standard

Even after considering corrections for the small angle scattering and the burnup, possible deviations can still occur in the density results. To account for the unknown sources of deviations an empirical correction factor, C_D , has been included in Eq. (2) and calculated using the sample standards as a reference. Limited to this experimental campaign, this factor has been calculated as the ratio between the lead density obtained from the densitometer, ρ_D , and the density obtained from the standards, ρ_{Std} , as:

$$C_D = \frac{\rho_{Std(Pb)}}{\rho_{D(Pb)}} \quad (6)$$

The motivation for using lead as a reference material is that lead compared to copper is closer to uranium dioxide in terms of atomic

Table 4

The table summarizes the beam parameters and the spatial resolution evaluated using the ESF 10–90%. The uncertainties have been calculated, for the count rate based on the Poisson statistics (Gilmore, 2008), while the resolution uncertainty has been considered equal to the step size of the movement mechanism.

Gamma line energy [keV]	1173	1332
Flat beam count rate 4 h [cps]	122.23(10)	119.99(9)
Flat beam test 1 [cps]	122.37(20)	120.67(19)
Flat beam test 2 [cps]	123.18(20)	120.89(19)
Flat beam test 3 [cps]	122.44(23)	120.50(21)
Bkg. count rate [cps]	0.21(2)	0.21(1)
ESF 10–90% [mm]	0.29(1)	0.28(1)

number and density. Nevertheless, this does not represent the ideal procedure: for future measurements, the used unirradiated sample of uranium oxide should be used instead to provide a more representative calibration sample. Further details for future calibration procedures are provided as an outlook in Section 6.

3.2. Note on the uncertainty estimation

The uncertainty of the density estimate, σ_ρ , was calculated using first-order error propagation, based on the respective uncertainties of flatfield intensity, transmitted intensity, and thickness measurement:

$$\sigma_\rho = \sqrt{\frac{\sigma_{I_0}^2}{(I_0 \mu_m x)^2} + \frac{\sigma_I^2}{(I \mu_m x)^2} + \left(\frac{\ln(I_0/I)}{x^2 \mu_m} \right)^2 \sigma_x^2}. \quad (7)$$

Where σ_{I_0} , σ_I and σ_x are the uncertainties respectively of the unattenuated and attenuated beam intensity and the sample thickness. The uncertainty of the correction factors has been considered negligible. To summarize the uncertainty estimation, an uncertainty budget is reported in Appendix A.

4. Results

4.1. Setup properties measurements

The results from the flat beam and background count rates and spatial resolution tests are summarized in Table 4 for both the gamma lines of interest. As mentioned in Section 2.2, a flat beam measurement of 4 h has been acquired and used in the density calculations. Three additional measurements (reported in Table 3) of about 1 h were also performed during the measurement campaign and used to test the beam stability and some fluctuations have been observed. These fluctuations were determined to be statistically significant using a χ^2 decision test (Wiss et al., 2017), which rejected the hypothesis that the intensity is stable across the different flat beam tests, with a 1% p-value. The consequences of this will be further discussed in Section 5.

The spatial resolution of the system has been evaluated using the response of the system to a sharp edge. The difference between the positions corresponding to 10% to 90% of the signal variation has been used as an estimate of the resolution as shown in Fig. 5. These positions have been evaluated by linear interpolation estimating a 10–90% edge spread of about 0.28 ± 0.01 mm for both the gamma lines of interest. The uncertainty was based on the precision of the positioning mechanism.

4.2. Calibration sample measurements

After alignment, a density calibration was performed by scanning the lead and copper calibration samples (Fig. 3b and c) along the stairs patterns for 12 min per position (one every 0.25 mm). The signal profiles

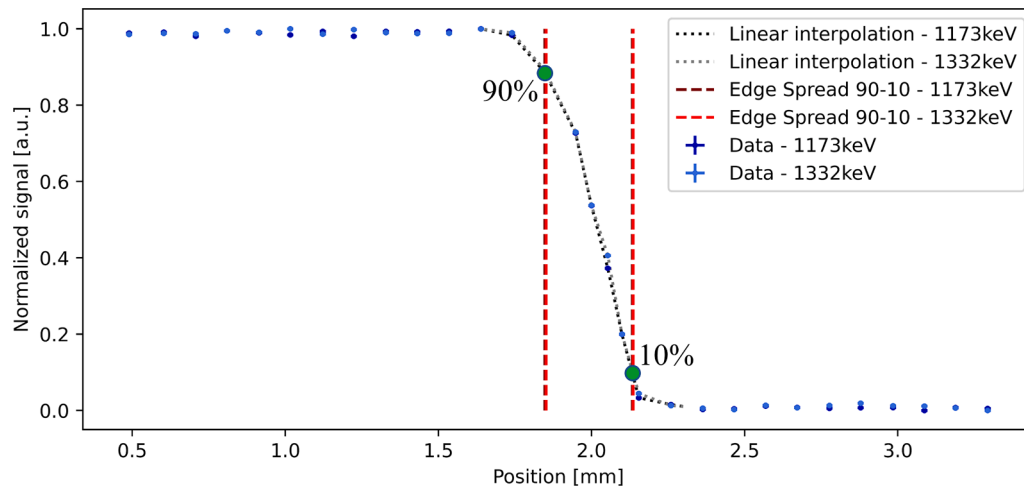


Fig. 5. The ESF data are reported for both energy lines. Linear interpolation was used to obtain a 10 to 90% edge spread and used as an estimate of the spatial resolution of the system. The position uncertainty is the fluctuation observed during the measurements, the signal uncertainty is derived from Poisson statistics.

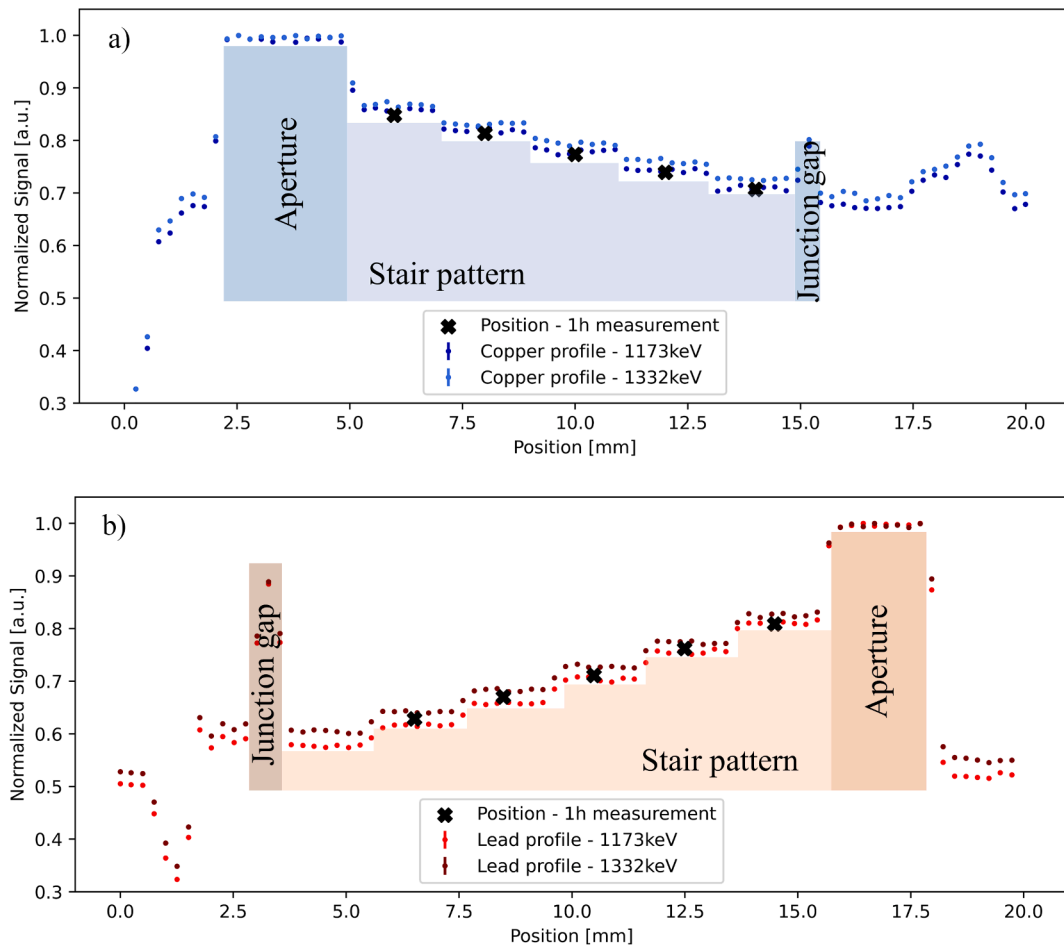


Fig. 6. Normalized signal profiles of the stairs pattern samples made of copper a) and lead b), obtained by dividing the signal profile for its maximum value. The stairs structure can be observed for both the gamma lines of interest, but also other features of the sample itself. At the extremities of the stairs pattern two increases of the signal can be observed: one due to the presence of an aperture at the end of the stairs (as can be seen from the sample images) and a second one at the other extremity, due to the “junction gap”, a gap sited between the stairs pattern structure and the rest of the sample object. The black crosses mark the positions where the 1 h measurements were taken and used to calculate the densities reported in Fig. 7.

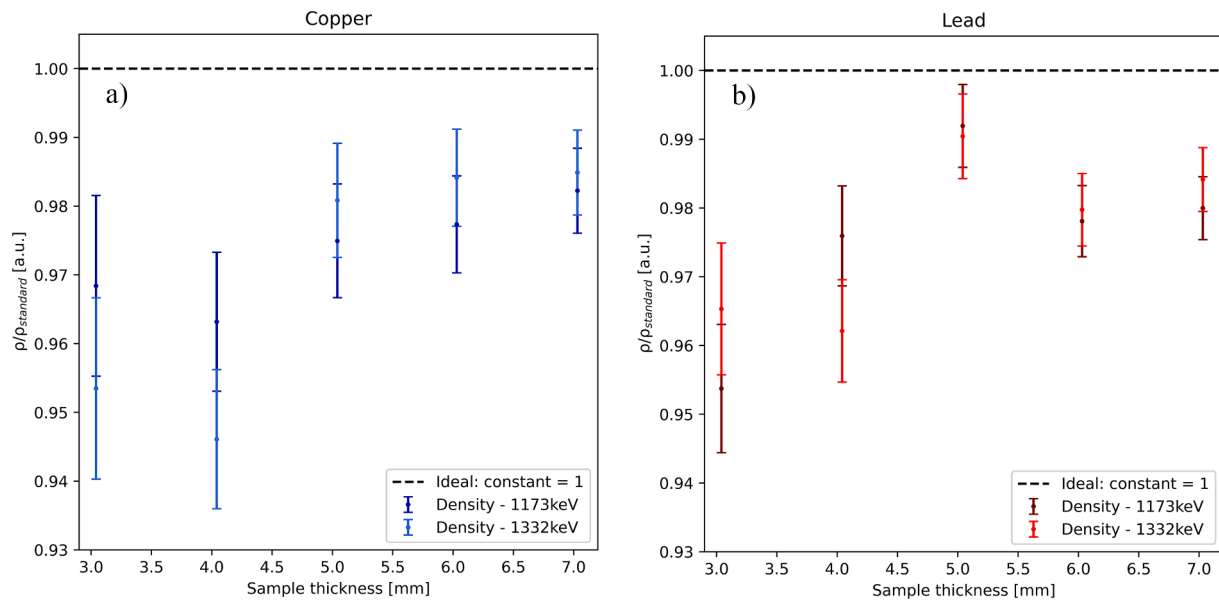


Fig. 7. Density ratio plot between the densitometer measurement and the sample standards for copper a) and lead b). The two color shades used in each plot represent correspond to the different gamma lines of Co-60 (1173 keV and 1332 keV). The error reported is for 1σ and evaluated by propagating the statistical uncertainty of the measured data and the uncertainty in the thickness measurements.

Table 5

The table reports the attenuation coefficients and the small angle correction factors used for calculating the density of the calibration samples for their different thicknesses (3, 4, 5, 6, and 7 mm). The attenuation factor, $\mu_{w.o.}$, was obtained from NIST-XCOM libraries (Berger et al., 2020) without coherent scattering. The small angle correction factors uncertainty reported was obtained from the MCNP simulations.

Material	Copper		Lead	
Gamma line energy [keV]	1173	1332	1173	1332
$\mu_{w.o.}$ [cm ² /g]	0.054	0.051	0.060	0.055
C_s				
Thickness [mm]	3	1.0093(4)	1.0075(4)	1.0312(5)
	4	1.0069(5)	1.0050(4)	1.0313(6)
	5	1.0054(5)	1.0036(5)	1.0320(6)
	6	1.0060(6)	1.0046(6)	1.0317(7)
	7	1.0064(6)	1.0048(6)	1.0318(8)

obtained, shown in Fig. 6a and b, were used to center the densitometer in the stairs' steps (marked with a black cross). From the signal profiles, the stairs structure and the aperture at the end of the stairs could be observed. A spike in the signal profile could be noticed after the thickest step of the stairs pattern. This was due to a small gap present between the first step and the round metal support since the calibration samples were made of two metal pieces (the stairs pattern and the round support) screwed together.

Repeated measurements of 1 h duration were used to calculate the density with high precision using Eq. (2). The ratio between the density measured with the densitometer and the density calculated using the reference standards (Fig. 3d) is shown in Fig. 7a (copper) and b (lead) as a function of the step thickness. It can be noted that for bigger thicknesses a slightly improved accuracy can be observed, with about 2% of deviations for thicknesses bigger than 5 mm, so in the fuel samples range. The correction factors described in Section 3.1 and used for the calculations are reported in Table 5.

4.3. Fuel sample measurements

The sample (shown in a schematic representation in Fig. 8a) has been

localized by using the signal variation caused by the presence of three different structures made of different materials: epoxy, Zircaloy-2®, and uranium dioxide. The irradiated fuel slice has been embedded in epoxy with its cladding and, by looking for the cladding position, also the fuel region would be identified. This has been searched with two scans in the diametral opposite sides of the sample. The left scan (indicated by the green arrow in Fig. 8b) has been acquired with 1 h measurement per position and a step size of 0.1 mm, while the right part of the scan (indicated by the violet arrow in Fig. 8b) has been acquired with sparser (0.150 mm step) and shorter measurements (280 s). The outer edge spread curve has been considered as the position of the start of the cladding for an estimated diameter of 9.58 ± 0.1 mm (declared at the fabrication of 9.62 mm).

The identification of the cladding position provided a reference also for evaluating the position of the fuel region. This has been considered by adding and subtracting the nominal cladding thickness (0.62 mm) from the left-hand and right-hand side of outer cladding positions, as shown in Fig. 8b. We are then assuming that the cladding thickness has not been altered significantly during the irradiation.

The long measurements performed on the rod sample have been used to estimate the density profile in the fuel region. The scan covers a radial range of 7.3 mm (which includes the proximity of region outside of the cladding till the center of the fuel pellet, with some margin), using a step size of 0.1 mm and 1 h of measurement time per step. For each position considered in the fuel region (yellow area in Fig. 8), the local density was calculated (using the parameters reported in Table 6), obtaining the fuel density profile shown in Fig. 9. To avoid the interferences of the signal due to edge spread from the fuel-cladding interface a margin has been considered from the cladding-pellet interface. This has been calculated as half of the ESF 10–90% and reported in Fig. 9. Only the measurement points above that position have been considered with limited interference from the lower density of the cladding (up to 10% for the first neighboring point).

The mean of the bulk density of the fuel was determined to be 9.58 ± 0.09 g/cm³ (1173 keV), and 9.57 ± 0.09 g/cm³ (1332 keV), where the reported uncertainty is the sample standard deviations. The measurement was compared with the density measured after irradiation, obtained through the immersion densitometry in decane (10.18 ± 0.03 g/cm³), showing a discrepancy of about 5.5%. The immersion measurement has been performed on another sample (a rod section of about 10

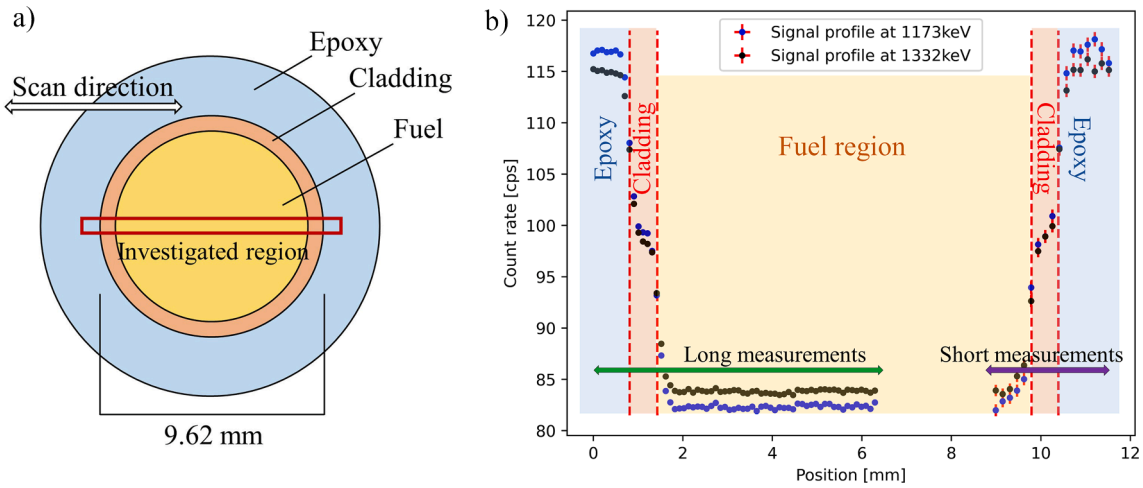


Fig. 8. a) A schematic drawing of the fuel sample is shown presenting the various elements with different color patterns: in blue the epoxy used to contain the rod element, in red the zircalloy® cladding and in yellow the fuel region, made of uranium dioxide. The same colors have been used to show the corresponding regions in the fuel scan shown in b). The different materials providing a different attenuation give a modulation in the signal, which indicates their positioning. Two arrows indicate which measurements have been acquired with a long (green – 1 h) or a short (violet – 280 s) measurement time.

Table 6

The table reports the correction factors and the attenuation coefficients used for calculating the density of the irradiated fuel sample. The attenuation factor, $\mu_{w.o.}$, was obtained from NIST-XCOM libraries (Hallman, 2020) without the coherent scattering for pure UO_2 . The uncertainties of the small angle scattering correction factor, C_S , were obtained from the MCNP simulations, while for calibration correction, C_D , the uncertainties were obtained from the lead measurements.

Material	ADOPT™-UO ₂	
Gamma line energy [keV]	1173	1332
$\mu_{w.o.}$ [cm^2/g]	0.064	0.058
C_S	1.0316(7)	1.0272(7)
C_U	1.0126	1.0108
C_D	1.0224(58)	1.0207(58)

mm taken from the same fuel rod but in a different location), measuring the fuel volume by subtracting the volume occupied by the cladding. It can be noted that the discrepancy observed can be partially explained by

the principles on which relies the methodologies themselves. In immersion densitometry, the fluid used for the immersion can penetrate big cracks and open porosities of the fuel and these features are not considered for the subsequent density calculation. Conversely, these features affect the density measured locally by the gamma densitometer, resulting in a lower average density.

With a close look at the density distribution reported in Fig. 9, two different features can be noticed:

1. Density decrease in rim: a significant decrease in density in the two outermost measurement points of the fuel scan has been observed. These two points are located in the fuel region and outside the region of interference due to the edge spread of the fuel-cladding interface. Such behavior could depend on a possible increase in the porosity fraction of the rim, but to ensure that this is the cause, complementary measurements (such as optical or electron microscopy (Szymańska et al., 2008) need to be used to validate this statement.
2. Local density drops: local density variations have been observed in the bulk of the fuel, mainly due to the statistical fluctuation of the

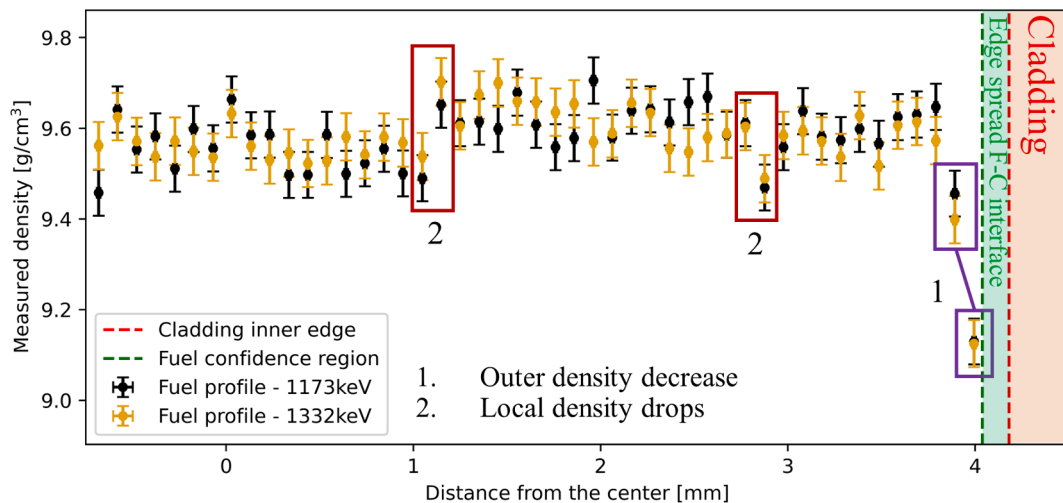


Fig. 9. The measured density profile of the irradiated fuel sample measured. The measurements are quite stable between ± 1.3 percent from the average value, except for the outermost measurement points. The uncertainties reported are 1σ uncertainty estimates according to Section 3.2.

data. However, it can be noticed that in a few locations, deviations bigger than one standard deviation could be observed, for both gamma-ray energies, which could also be a possible sign of a local density drop. However, this has not been confirmed by any independent analysis.

5. Conclusion and discussion

A prototype of a novel gamma transmission micro-densitometer was realized in Studsvik laboratories, and a test campaign was executed, demonstrating the feasibility of the proposed application. Through the alignment procedure, a collimated beam was obtained showing an intensity sufficient to perform the transmission measurements in sub-percent level precision and with fine enough collimation for resolution in the 100- μm range.

During the acquisition campaign, a 4 h flatfield count rate measurement was used, which showed intensity in the same order of magnitude as predicted (Senis et al., 2021). The flatfield stability was tested with three additional measurements of about 1 h. We can conclude that the fluctuation observed in the flatfield intensity cannot be explained only by the statistical uncertainties. One possible explanation could be the stability of the detector itself: studies demonstrated the stability of an HPGe detector could be obtained at 0.4% level (Szymańska et al., 2008), however, the long-term stability of the beam intensity and detector needs to be further investigated.

The spatial resolution of the setup was obtained by measuring the ESF 10–90% which was about 0.28 ± 0.01 mm for both the gamma lines used. This value was bigger than the predicted, (Senis et al., 2021) but still suitable for sub-millimetric investigations. The double collimator configuration as used in the measurement campaign increases the spread of the field of view in the vertical direction (which is the same direction as the sample movement). A path for further improving this performance is thus outlined. Some influence could also be expected as a consequence of the manual procedures used for the setup alignment and in the sample positioning.

Two calibration samples of copper and lead were used to evaluate the density results measured with the densitometer. The measurements performed at different sample thicknesses were compared to their material standards. The comparison showed a bigger deviation for lower thicknesses (with a maximum of 5%) but smaller (about 2%) for thicknesses that are of interest for the irradiated fuel samples. The deviations obtained for the lead sample were used for calibration of the densitometer for use on uranium oxide fuel. However, further work is needed to carefully examine the possibility of a remaining bias affecting the measurements.

An irradiated ADOPTTM fuel sample with an average burnup of 65 GWd/tU was inspected with the technique. The fuel bulk density obtained was 9.58 ± 0.09 g/cm³ (at 1173 keV), and 9.57 ± 0.09 g/cm³ (at 1332 keV). These results showed a lower density (about 5.5%) if compared with the density calculated using immersion densitometry in decane. A cause for deviation is possibly due to the methodologies themselves, where fuel volume considered by immersion densitometry is lower due to e.g. fluid penetration in cracks and open porosities. The radial density profile also showed the presence of local density drops, which could be explained by known features observed in irradiated fuel samples (such as rim effects or cracks). However, the accuracy of the densitometer needs extensive testing, especially regarding the accuracy of the measurements on irradiated fuel samples. Furthermore, the correlation between the observations in the density profile and the suggested causes needs to be proven with other methodologies.

6. Outlook

This work represents the first experimental campaign with this novel

gamma densitometry setup and some improvements can be suggested for the further development of the technique.

Reproducibility: Some weaknesses have been identified regarding the reproducibility of the measurements due to the preparation and procedures needed to run the setup. Manual manipulation is needed, such as in the alignment procedure and the sample changing and positioning. Finding an alternative approach is challenging, since, in a hot cell, changes in the setup need to be carefully planned. A series of measurements on an unirradiated uranium dioxide sample is recommended in order to examine the reproducibility of the ESF and the density obtained.

Flat field stability: It was found that additional sources of uncertainty affect the flat beam, other than counting statistics. The cause of this is at the moment unclear. Stability tests can be used to exclude the detector as the cause of these fluctuations, by performing repeated measurements with a test source and evaluating the detector's stability over time. In general, HPGe detectors are stable, but it should be remembered that, in this application, high precision is aimed. The fluctuation observed between the four performed flat beam tests was at the 0.8 % level.

Spatial resolution: Furthermore, it has been noted that rotating the collimators 90° degrees such that the nearer collimator defines the resolution in the direction of the scan should improve the spatial resolution, since the divergence of the field of view of a collimator increases with the distance from it.

CRedit authorship contribution statement

L. Senis: Conceptualization, Methodology, Software, Investigation, Visualization, Formal analysis, Resources, Writing – original draft. **V. Rathore:** Resources, Writing – review & editing. **P. Andersson:** Supervision, Conceptualization, Funding acquisition, Resources, Writing – review & editing. **K. Johnson:** Supervision, Conceptualization, Investigation, Funding acquisition, Resources, Writing – review & editing. **D. Jädnäs:** Supervision, Conceptualization, Investigation, Resources, Writing – review & editing, Funding acquisition. **C. Losin:** Funding acquisition. **D. Minghetti:** Conceptualization, Supervision, Investigation, Resources, Writing – review & editing. **J. Wright:** Resources, Writing – review & editing. **D. Schrire:** Conceptualization, Resources, Writing – review & editing.

Declaration of Competing Interest

The authors declare that they have no known competing financial interests or personal relationships that could have appeared to influence the work reported in this paper.

Data availability

Data will be made available on request.

Acknowledgments

This work was financially supported by the Swedish Foundation for Strategic Research, grant number EM-16-0031, and the Pre-HALTED project members: Studsvik AB, Westinghouse Electric Sweden AB, Vattenfall Nuclear Fuel AB, and Uppsala University. A special thank also goes to all the technicians and engineers in Studsvik that helped with their technical support in the realization of this measurement campaign.

Appendix A

The uncertainty budget is presented in Table 7.

Table 7

The table reports the uncertainty sources considered and their estimates.

Parameter	Evaluation method		Estimated relative uncertainty contribution to the density evaluation	Subject to correction?
Counting statistics	Experimentally	Evaluated experimentally as described in Eq. (7).	0.8%	No
Calibration bias	Experimentally	Evaluated experimentally using a well-characterized calibration sample of lead.	2.5%	Yes
Collimator alignment	–	A misalignment in the collimation might degrade the spatial resolution but is not expected to generate a bias in the density measurement.	–	–
Sample dimensions	Machining precision	Calculated according to Eq. (7), based on the precision in machining of the metal samples and the fuel pellet, which is less than 0.01 mm.	0.1% – 0.3%	No
Sample tilt	Geometrical model	Bias generated in the case of sample tilt in the sample holder. A rotation of 1° has been assumed along the y-axis (Fig. 2 reference system).	0.01%	No
Coherent scattering	MC model	The coherent scattering generates a bias in measurement and has been evaluated using MCNP as explained in Section 3.1.1.	< 1% (Cu) < 3% (Pb)	Yes
Burnup correction	Fit model	The burnup bias is described in Section 3.1.2 and Ref. (Atak et al., 2020).	1% (at 65 GWd/tU)	Yes*

* Note that the burnup degradation of the attenuation coefficient is corrected according to average burnup, which may lead to an underestimate of density by up to 1% in the high burnup rim.

References

- Affonso R.R.W., da Silva A. X., Salgado C. M., Gamma ray densitometry techniques for measuring of volume fractions. In: *INAC 2015: International Nuclear Atlantic Conference. Brazilian Nuclear Program. State Policy for a Sustainable World*, Sao Paulo, SP (Brazil), 2015, URL <https://inis.iaea.org/search/search.aspx?orig.q=RN:47035607>.
- Atak H., Anastasiadis A., Jansson P., Elter Z., Andersson Sundén E. et al., 2020. The degradation of gamma-ray mass attenuation of UOX and MOX fuel with nuclear burnup, *Progr. Nucl. Energy*, 125, 103359, <https://doi.org/10.1016/j.pnucene.2020.103359>.
- Barlow, R.J., 1993. *Statistics: A Guide to the Use of Statistical Methods in the Physical Sciences*. Wiley.
- Baron, D.D., Hallstadius, L., 2012. Fuel performance of light water reactors (uranium oxide and MOX). In: *Comprehensive Nuclear Materials*. Elsevier, Oxford, pp. 481–514.
- Baron, D., Kinoshita, M., Thevenin, P., Largenton, R., 2009. Discussion about HBS transformation in high burn-up fuels. *Nucl. Eng. Technol.* 41 (2), 199–214. <https://doi.org/10.5516/NET.2009.41.2.199>.
- Berger M.J., Hubbell J.H., Seltzer S.M., Chang J., Coursey J.S., Sukumar R., Zucker D.S., Olsen K., XCOM: Photon Cross Section Database (version 1.5), Gaithersburg, 2020.
- Caruso, S., Murphy, M.F., Jatuff, F., Chawla, R., 2008. Nondestructive determination of fresh and spent nuclear fuel rod density distributions through computerised gamma-ray transmission tomography. *J. Nucl. Sci. Technol.* 45 (8), 828–835. <https://doi.org/10.1080/18811248.2008.9711484>.
- Caruso, D., Murphy, M.F., Jatuffa, F., Chawlaab, R., 2009. Determination of within-rod caesium and europium isotopic distributions in high burnup fuel rods through computerised gamma-ray emission tomography. *Nucl. Eng. Design* 239 (7), 1220–1228. <https://doi.org/10.1016/j.nucengdes.2009.02.019>.
- Caruso S., Characterisation of High-Burnup LWR Fuel Rods through Gamma Tomography, Lausanne, EPFL, 2007, THÈSE NO 3762.
- Daniel R.C., Bleiberg M.L., Meieran H.B., Yeniscavich W., Effects of High Burnup on Zircaloy-Clad Bulk UO₂, Plate Fuel Element Samples, United States, 1962, URL <https://www.osti.gov/biblio/4747035>.
- Díaz, J., Kimb, T., Petrova, V., Manera, A., 2021. X-ray and gamma-ray tomographic imaging of fuel relocation inside sodium fast reactor test assemblies during severe accidents. *J. Nucl. Mater.* 543, 152567 <https://doi.org/10.1016/j.jnucmat.2020.152567>.
- Gilmore, G.R., 2008. *Practical Gamma-ray Spectroscopy*, Nuclear Training Services Ltd, Warrington. Wiley, UK.
- Guerin, Y., 2012. Fuel performance of fast spectrum oxide fuel. In: *Comprehensive Nuclear Materials*. Elsevier, pp. 547–578.
- Hallman L.H. Jr et al., Advanced doped pellet technology (ADOPTM) fuel, Westinghouse Electric Company LLC, Cranberry Township, PA 16066, USA, 2020, URL: <https://www.nrc.gov/docs/ML2013/ML20132A014.pdf>.
- Kumara, W.A.S., Halvorsen, B.M., Melaaen, M.C., 2010. Single-beam gamma densitometry measurements of oil–water flow. *Int. J. Multiphase Flow* 36 (6), 467–480. <https://doi.org/10.1016/j.ijmultiphaseflow.2010.02.003>.
- Lassahn, G.D., Stephens, A.G., Taylor, D.J., Wood, D.B., 1979. “X-ray and gamma ray transmission densitometry. International colloquium on densitometry. Idaho Falls, ID, USA <http://inis.iaea.org/Search/search.aspx?orig.q=RN:11500068>.
- Lee, B.H., Koo, Y.H., Sohn, D.S., 2001. Rim characteristics and their effects on the thermal conductivity in high burnup UO₂ fuel. *J. Nucl. Sci. Technol.* 38 (1), 45–52. <https://doi.org/10.1080/18811248.2001.9715006>.
- Lozano, N., Desgranges, L., Aymes, D., Niepce, J.C., 1998. High magnification SEM observations for two types of granularity in a high burnup PWR fuel rim. *J. Nucl. Mater.* 257 (1), 78–87. [https://doi.org/10.1016/S0022-3115\(98\)00056-7](https://doi.org/10.1016/S0022-3115(98)00056-7).
- Noiroi, J., Desgranges, L., Lamontagne, J., 2008. Detailed characterisations of high burn-up structures in oxide fuels. *J. Nucl. Mater.* 372 (2), 318–339. <https://doi.org/10.1016/j.jnucmat.2007.04.037>.
- Pasalic, M., Rustempasic, F., Iyengar, S., Melin, S., Noah, E., 2014. Fatigue testing and microstructural characterization of tungsten heavy alloy Densimet 185. *Int. J. Refract. Metals Hard Mater.* 42, 163–168. <https://doi.org/10.1016/j.jrmhm.2013.09.001>.
- Reilly D., Ensslin N., Smith H. Jr., Kreiner S., Passive Nondestructive Assay of Nuclear Materials, US Nuclear Regulatory Commission Report NUREG/CR-5550 and Los Alamos National Laboratory Report LA-UR-90-732, 1991, URL: https://www.lanl.gov/orgs/n/n1/FMTTD/neut_mc/pdfs/LA_UR_90_0732.pdf.
- Rondinella, V.V., Wiss, T., 2010. The high burn-up structure in nuclear fuel. *Mater. Today* 13 (12), 24–32. [https://doi.org/10.1016/S1369-7021\(10\)70221-2](https://doi.org/10.1016/S1369-7021(10)70221-2).
- Schopper, H., 1957. Die elastische Streuung von γ -Strahlen bei kleinen Streuwinkeln. *Zeitschrift für Physik* 147 (3), 253–260. <https://doi.org/10.1007/BF01333094>.
- Schrire D., Kindlund A., Ekberg P., OECD Halden Reactor Project, Enlarged Halden Programme Group Meeting on High Burn-up Fuel Performance, Safety and Reliability and Degradation of In-Core Materials and Water Chemistry Effects, Vol I, HPR-349, Lillehammer, Norway, 15–20 March 1998, URL <http://inis.iaea.org/Search/search.aspx?orig.q=RN:35048536>.
- Senis, L., Rathore, V., Jansson, P., Andersson, P., Johnson, K., Jädnäs, D., Losin, C., Minghetti, D., Schrire, D., 2021. Feasibility study of gamma-ray micro-densitometry for the examination of nuclear fuel swelling. In: *Top Fuel 2021*, Santander, Spain, pp. 24–28 <http://urn.kb.se/resolve?urn=urn:nbn:se:uu:diva-442645>.
- Senis, L., Elter, Z., Rathore, V., Andersson Sundén, E., Jansson, P., Holcombe, S., Åberg Lindell, M., Håkansson, A., Andersson, P., 2022. A computational methodology for estimating the detected energy spectra of the gamma-ray flux from irradiated nuclear fuel. *IEEE Trans. Nucl. Sci.* 69 (4), 703–713. <https://doi.org/10.1109/TNS.2022.3152264>.
- Spino, J., Vennix, K., Coquerelle, M., 1996. Detailed characterisation of the rim microstructure in PWR fuels in the burn-up range 40–67 GWd/tM. *J. Nucl. Mater.* 231 (3), 179–190.
- Spino, J., Baron, D., Coquerelle, M., Stalios, A.D., 1998. High burn-up rim structure: evidences that xenon-depletion, pore formation and grain subdivision start at different local burn-ups. *J. Nucl. Mater.* 256 (2), 189–196. [https://doi.org/10.1016/S0022-3115\(98\)00060-9](https://doi.org/10.1016/S0022-3115(98)00060-9).
- Spino, J., Rest, J., Goll, W., Walker, C.T., 2005. Matrix swelling rate and cavity volume balance of UO₂ fuels at high burn-up. *J. Nucl. Mater.* 346 (2), 131–144. <https://doi.org/10.1016/j.jnucmat.2005.06.015>.
- Storruste, A., Tjöm, P.O., 1958. Small angle scattering of 1.33 MeV and 1.17 MeV gamma rays. *Nucl. Phys.* 6, 151–156. [https://doi.org/10.1016/0029-5582\(58\)90094-4](https://doi.org/10.1016/0029-5582(58)90094-4).
- Swinehart, D.F., 1962. The Beer-Lambert Law. *J. Chem. Educ.* 39 (7), 333–335. <https://doi.org/10.1021/ed039p333>.
- Szymańska, K., Achenbach, P., Agnello, M., Botta, E., Bracco, A., Bressani, T., Camera, F., Cederwall, B., Feliciello, A., Ferro, F., Gerl, J., Iazzi, F., Kavatsyuk, M., Kojouharov, I., Pochodzalla, J., Raciti, G., Saito, T.R., Sanchez Lorente, A., Tegnér, P.-E., Wieland, O., 2008. Resolution, efficiency and stability of HPGe detector operating in a magnetic field at various gamma-ray energies. *Nucl. Instrum. Methods Phys. Res. Sect. A: Accel. Spectrom. Detect. Assoc. Equip.* 592 (3), 486–492.
- Tjugum, S.A., Frieling, J., Johansen, G.A., 2002. A compact low energy multibeam gamma-ray densitometer for pipe-flow measurements. *Nucl. Instrum. Methods Phys. Res. B* 197 (3), 301–309. [https://doi.org/10.1016/S0168-583X\(02\)01481-7](https://doi.org/10.1016/S0168-583X(02)01481-7).

- Une, K., Nogita, K., Kashibe, S., Imamura, M., 1992. Microstructural change and its influence on fission gas release in high burnup UO₂ fuel. J. Nucl. Mater. 188, 65–72. [https://doi.org/10.1016/0022-3115\(92\)90455-T](https://doi.org/10.1016/0022-3115(92)90455-T).
- Van Brutzel L., Dingreville R., Bartel T.J., Nuclear fuel deformation phenomena. In: *in State of the Art Report on Multi-scale Modelling of Nuclear Fuels*, 2015, pp. 59-79, URL https://inis.iaea.org/search/search.aspx?orig_q=RN:47032408.
- Werner, C.J., 2017. MCNP User's Manual - Code Version 6.2. Report LA-UR-17-29981. Los Alamos National Laboratory.
- Wiss T. et al., 2017. Properties of the high burnup structure in nuclear light water reactor fuel, *Radiochim. Acta*, 105(11) 893–906.